Real-time Calculation of a Limiting form of the Renyi Entropy Applied to Detection of Subtle Changes in Scattering Architecture

M.S. Hughes[1], J.E. McCarthy[2], M.V. Wickerhauser[2], J.N Marsh[1], J.M. Arbeit[1],
R.W. Fuhrhop[1],K.D. Wallace[1], T. Thomas[1], J. Smith[1], K. Agyem[1], G. M. Lanza[1], and S. A. Wickline[1]
[1] *Washington University School of Medicine*
[2] *Department of Mathematics, Washington University*

(Dated: March 31, 2009)

Previously we reported a new method for ultrasound signal characterization using entropy, H_f, and demonstrated that in certain settings, further improvements in signal characterization could be obtained by generalizing to Renyi Entropy-based signal characterization, $I_f(r)$ with values of r near 2 (specifically $r = 1.99$)[1]. We speculated that further improvements in sensitivity might be realized at the limit $r \to 2$. At that time, such investigation was not feasible due to excessive computational time required to calculate $I_f(r)$ near this limit. In this paper, we now derive an asymptotic expression for the limiting behavior of $I_f(r)$ as $r \to 2$ and present results analogous to those obtained with $I_f(1.99)$. Moreover, the limiting form, $I_{f,\infty}$ is computable directly from the experimentally measured waveform, $f(t)$ by an algorithm that is suitable for real-time calculation and implementation.

PACS numbers:

I. INTRODUCTION

In an earlier paper[1] we reported on the application of Renyi entropy, $I_f(r)$ which is defined for all $r < 2$ (r is roughly a reciprocal "temperature"), for the detection of changes in backscattered RF arising from the accumulation of targeted nanoparticles in the neovasculature in the insonified region of a tumor. That study was motivated by the observation that acoustic characterization of sparse collections of targeted perfluorocarbon nanoparticles presented challenges that might require the application of novel types of signal processing[2]. We were able to show that signal processing based on a "moving window" H_f analysis (see Eq. (7)) could detect accumulation of tissue-targeted nanoparticles 30 minutes following nanoparticle injection. The signal energy, defined as the sum of squares of the over the same moving window, was unable to distinguish measurements made at any time during the one hour experiment (as was conventional B-mode imaging). Subsequently we determined that "moving window" $I_f(r)$ analysis, with $r = 1.99$, could distinguish the difference in backscatter measured at 0 and 15 minutes. Reduction of the accumulation time required to reach detectability from 30 to 15 minutes is clearly of significance: potentially reducing both patient discomfort and increasing clinical throughput. Moreover, although the computational effort to obtain the result precluded its clinical application with currently available equipment, the study raised the possibility of further sensitivity improvements by using values of r closer to the limiting value of 2, where $I_f(r)$ approaches infinity. The purpose of the current study is to investigate the behavior of $I_f(r)$ as $r \to 2$ by extracting its asymptotic form. While this involves use of the first derivatives of $f(t)$ at its critical points, which can be expected to increase noise in the processing chain output, surprisingly the resulting signal processing scheme does not sacrifice sensitivity. Moreover, the operation count in this approach is lower than

that used to produce the signal envelope, which currently is the standard for real-time ultrasonic imaging display, thus demonstrating its suitability for implementation in a real-time imaging system.

II. APPROACH

All results in this study were obtained using the density function, $w_f(y)$ of the continuous function $y = f(t)$, assumed to underlie the sampled RF data. Subsequently, $w_f(y)$ was used to compute the entropy $I_f(r)$. As described in previous studies $w_f(y)$ corresponds to the density functions used in statistical signal processing[1]. In contradistinction to statistical signal processing, where $f(t)$ is a random function, and often nowhere differentiable, we assume that the noise levels in our apparatus are low enough so that with sufficient signal averaging, noise may be eliminated, or at least reduced to a low enough level, that derivatives of $f(t)$ may be accurately computed. From these derivatives the density function $w_f(y)$ may be computed[1], which then facilitates calculation of the quantities typically discussed in statistical signal processing (*e.g.*, mean values, variances, covariances)[3–5]. However, in that environment, the density function is usually assumed to be continuous, infinitely differentiable, and to approach zero at infinity. In our case $w_f(y)$ is not so well-behaved and has (integrable) singularities. While this renders calculation of the density function more difficult, applications of entropy imaging based on $w_f(y)$ have shown the cost to be justified in terms of increased sensitivity to subtle changes in scattering architecture that are often undetected by more conventional imaging.

We use the same conventions as in previous studies so

that

$$w_f(y) = \sum_{k=1}^{N} |g'_k(y)|, \qquad (1)$$

where N is the number of laps (regions of monotonicity of $f(t)$), $g_k(y)$ is the inverse of $f(t)$ in the kth-lap and if y is not in the range of $f(t)$ in the kth-lap, $g'_k(y)$ is taken to be 0.

We also assume that all experimental waveforms $f(t)$ have a Taylor series expansion valid in the domain: $[0, 1]$. Then near a time t_k such that $f'(t_k) = 0$

$$y = f(t) = f(t_k) + \frac{1}{2!} f''(t_k)(t - t_k)^2 + \cdots, \qquad (2)$$

where t_k is a lap boundary. On the left side of this point Eq. (2) may be truncated to second order and inverted to obtain

$$g_k(y) \sim t_k \pm \sqrt{2(y - f(t_k))/f''(t_k)}, \qquad (3)$$

with

$$|g'_k(y)| \sim 1/\sqrt{2f''(t_k)(y - f(t_k))}. \qquad (4)$$

The contribution to $w_f(y)$ from the right side of the lap boundary, from $g_{k+1}(y)$, is the same, so that the over-all contribution to $w_f(y)$ coming from the time interval around t_k is

$$|g'_k(y)| \sim \sqrt{2/(f''(t_k)(y - f(t_k)))}, \qquad (5)$$

for $0 < f(t_k) - y \ll 1$ for a maximum at $f(t_k)$ and $0 < y - f(t_k) \ll 1$ for a minimum. Thus, $w_f(y)$ has only a square root singularity (we have assumed that t_k is interior to the interval $[0, 1]$; if not, then the contributions to w_f come from only the left or the right). If, additionally, $f''(t_k) = 0$, then the square root singularity in Eq. (4) will become a cube-root singularity, and so on, so that the density functions we consider will have only integrable algebraic singularities.

Figure (1) illustrates the integrable singularities. In general, two types of behavior are possible in $w_f(y)$: discontinuities (not shown in the figure) and the integrable singularities shown in the figure. This figure shows that the density functions possess significantly different attributes from those usually considered in statistical signal processing. The mathematical characteristics of the singularities are important in order to guarantee the existence of the following integral on which we base our analysis of signals in this study:

$$I_f(r) = \frac{1}{1-r} \log \left[\int_{f_{min}}^{f_{max}} w_f(y)^r dy \right], \qquad (6)$$

which known as the Renyi entropy[6]. It is similar to the partition function in statistical mechanics with the parameter r playing the role of a reciprocal temperature[1,7], moreover, $I_f(r) \to -H_f$, as $r \to 1$, using L'Hôpital's rule, so that I_f is a generalization of H_f:

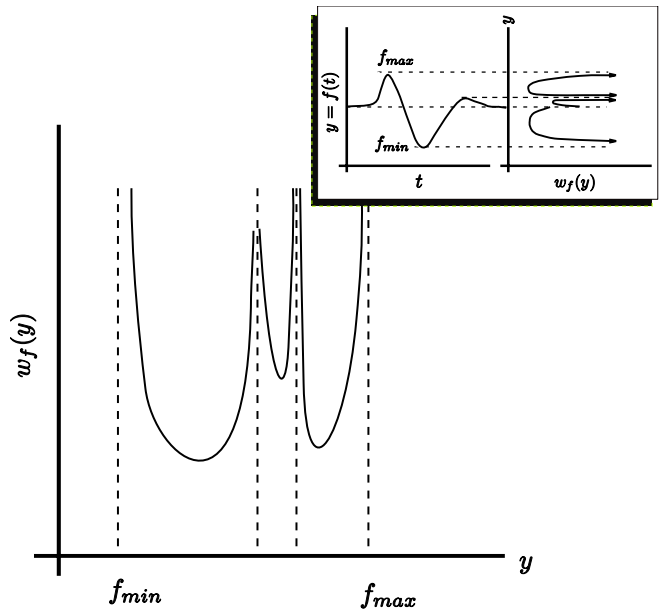$$H_f = \int_{f_{min}}^{f_{max}} w_f(y) \log w_f(y) dy. \qquad (7)$$

FIG. 1. A plot of a typical density function $w_f(y)$ employed in our study. Compared to the distribution functions typically encountered in statistical signal processing the function is ill-behaved, not even being continuous. Inset: A time-domain waveform, $f(t)$ with three critical points(left), and its associated density function $w_f(y)$ showing how the singularities relate to the critical points of the sampled waveform $f(t)$.

Previous studies have shown this quantity can be more sensitive to subtle changes in scattering architecture than are more commonly used energy-based measures,[2] with subsequent studies demonstrating further sensitivity improvements using I_f at the suitable value of r.[1] For the density functions $w_f(y)$ encountered in our study, $I_f(r)$ is undefined for $r \geq 2$, since as $r \to 2^-$, the integral appearing in Eq. (6) will grow without bound due to the singularities in the density function, $w_f(y)$ described by Eq. (5). The behavior as $r \to 2$ is dominated by contributions from these singularities, all of which correspond to critical points of $f(t)$. This behavior is shown in Figure (2). Moreover, as shown in the figure it is possible that two slightly different functions, $f(t)$ and $f(t) + \xi(t)$, where ξ is small, may have entropies, H_f and $H_{f+\xi}$ that are close, as shown, but whose Renyi entropies, $I_f(r)$ and $I_{f+\xi}(r)$ diverge as $r \to 2$. Previous studies have shown that this can happen in practice[1]. However, these results left open the possibility of further sensitivity gains. The purpose of the present study is to investigate the possibility of obtaining further sensitivity improvements by pushing toward this limit. To do this we will utilize the limiting form of $I_f(r)$ as $r \to 2$, which may be obtained by first observing that the integral in Eq. (6) may split into two parts, one corresponding to the region where the function is clearly bounded and one corresponding to its
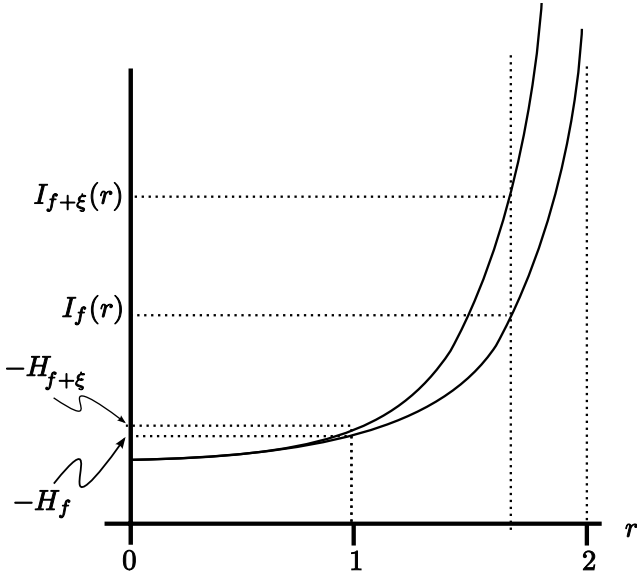
FIG. 2. Plots of $I_f(r)$ and $I_{f+\xi}(r)$ (left) showing that while $I_f(1) = -H_f$ and $I_{f+\xi}(1) = -H_{f+\xi}$ may be close, $I_f(r)$ and $I_{f+\xi}(r)$ diverge as $r \to 2$.
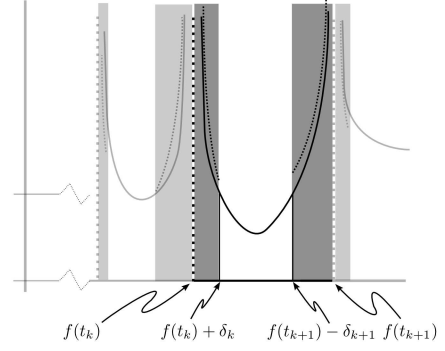

FIG. 3. An enlarged plot of a singularity of the density function $w_f(y)^{2-\epsilon}$ (solid curve) and Eq. (5) (dashed curves); quantities relevant for derivation of Eq. (19). As the shaded regions shrink the ratio between the dashed and solid curves approaches 1. The darker shading corresponds to the region discussed in the text.

singularities as shown in Figure (3). Thus,

$$
\int_{f(t_k)}^{f(t_{k+1})-\delta_{k+1}} w_f(y)^{2-\epsilon} dy =
$$
$$
= \int_{f(t_k)}^{f(t_k)+\delta_k} w_f(y)^{2-\epsilon} dy + \int_{f(t_k)+\delta_k}^{f(t_{k+1})-\delta_{k+1}} w_f(y)^{2-\epsilon} dy
$$
$$
= \int_{f(t_k)}^{f(t_k)+\delta_k} w_f(y)^{2-\epsilon} dy + B_k, \qquad (8)
$$

where we have written B_k for the integral over the unshaded region between $f(t_k) + \delta_k$ and $f(t_{k+1}) - \delta_{k+1}$ in Figure (3). We observe that B_k is bounded as $\epsilon \to 0$, while the integral appearing in Eq. (8) is not.

Next, we consider the small interval of length δ_k near the singularity of $w_f(f(t_k))$ (shaded regions of Figure (3)). This is the singularity corresponding to the kth extrema of $f(t)$: $f(t_k)$; also shown is the adjacent singularity corresponding to an extrema of $f(t)$ at t_{k+1}. The dashed lines in these regions represent the one over square root limiting form described in Eq. (5). By choosing δ_k small enough we may make the ratio of the solid and dashed curves arbitrarily close to one. In other words, Eqs. (1) and (5) tell us that in these shaded regions the following difference can be made as small as we like:

$$
\left| w_f(y - \delta_k) / \frac{a_k}{\sqrt{y - f(t_k)}} - 1 \right|, \qquad (9)
$$

where $a_k = \sqrt{2/f''(t_k)} = \sqrt{2/|f''(t_k)|}$ (assuming a minimum at $f(t_k)$; the argument for a maximum is similar). Moreover, if a particular choice of δ_k yields the desired accuracy, i.e., makes the difference enough small enough, choosing a smaller value of δ_k will produce greater accuracy. Since the number of extrema in our time domain

function $f(t)$ is finite, we pick the minimum δ_k, call it δ, yielding the desired accuracy in all of the shaded regions (i.e., at all singular points of $w_f(y)$). With this choice of δ Eq. (8) becomes

$$
\int_{f(t_k)}^{f(t_{k+1})-\delta} w_f(y)^{2-\epsilon} dy =
$$
$$
= \int_{f(t_k)}^{f(t_k)+\delta} w_f(y)^{2-\epsilon} dy + \tilde{B}_k, \qquad (10)
$$

and Eq. (9) becomes,

$$
\left| w_f(y - \delta) / \frac{a_k}{\sqrt{y - f(t_k)}} - 1 \right| < E, \qquad (11)
$$

or

$$
w_f(y - \delta) / \frac{a_k}{\sqrt{y - f(t_k)}} = 1 \pm E(y), \qquad (12)
$$

where $E > |E(y)|$ may be chosen to be as small as we like by choosing small enough δ. As a result

$$
w_f(y - \delta)^{2-\epsilon} = \frac{a_k}{\sqrt{y - f(t_k)}}^{2-\epsilon} [1 \pm E(y)]^{2-\epsilon}
$$
$$
= \frac{a_k}{\sqrt{y - f(t_k)}}^{2-\epsilon} [1 \pm \tilde{E}(y)], \qquad (13)
$$

where, once again, $\tilde{E}(y)$ is may be made arbitrarily small, i.e., for every $\tilde{E} > 0$ there exists some $\delta > 0$ such that $\tilde{E} > |\tilde{E}(y)|$ for all y in between $f(t_k)$ and $f(t_k) + \delta$. Combining Eqs. (10) and (13) now yields

$$\int_{f(t_k)}^{f(t_k)+\delta} w_f(y)^{2-\epsilon}dy + \tilde{B}_k =$$

$$= \int_{f(t_k)}^{f(t_k)+\delta} \left(\frac{a_k}{\sqrt{y-f(t_k)}} \right)^{2-\epsilon} \left[1 \pm \tilde{E}(y) \right] dy + \tilde{B}_k$$

$$= \int_{f(t_k)}^{f(t_k)+\delta} \left(\frac{a_k}{\sqrt{y-f(t_k)}} \right)^{2-\epsilon} dy$$

$$\pm \int_{f(t_k)}^{f(t_k)+\delta} \left(\frac{a_k}{\sqrt{y-f(t_k)}} \right)^{2-\epsilon} \tilde{E}(y)dy + \tilde{\tilde{B}}_k \quad (14)$$

The second integral above may be bounded by

$$\left| \int_{f(t_k)}^{f(t_k)+\delta} \left(\frac{a_k}{\sqrt{y-f(t_k)}} \right)^{2-\epsilon} \tilde{E}(y)dy \right| \leq$$

$$\leq \int_{f(t_k)}^{f(t_k)+\delta} \left(\frac{a_k}{\sqrt{y-f(t_k)}} \right)^{2-\epsilon} |\tilde{E}(y)|dy$$

$$\leq \int_{f(t_k)}^{f(t_k)+\delta} \left(\frac{a_k}{\sqrt{y-f(t_k)}} \right)^{2-\epsilon} \tilde{E}dy$$

$$\leq \tilde{E} \int_{f(t_k)}^{f(t_k)+\delta} \left(\frac{a_k}{\sqrt{y-f(t_k)}} \right)^{2-\epsilon} dy. \quad (15)$$

This inequality may be converted to an equality by replacing the $\tilde{E}$ factor by a smaller (positive) number. In general, this number will depend on the behavior of $w_f(y)$ near the singular point $y = f(t_k)$. For clarity, we denote this constant by $\tilde{E}_k$. With this notation, Eqs. (15) become

$$\int_{f(t_k)}^{f(t_k)+\delta} \left(\frac{a_k}{\sqrt{y-f(t_k)}} \right)^{2-\epsilon} \tilde{E}(y)dy =$$

$$\tilde{E}_k \int_{f(t_k)}^{f(t_k)+\delta} \left(\frac{a_k}{\sqrt{y-f(t_k)}} \right)^{2-\epsilon} dy \quad (16)$$

where $\tilde{E} \geq \tilde{E}_k > 0$ and hence may also be made as small as we wish by reducing δ. The common integral appearing in Eqs. (14) and (15) may be computed as

$$\int_{f(t_k)}^{f(t_k)+\delta} \left(\frac{a_k}{\sqrt{y-f(t_k)}} \right)^{2-\epsilon} dy =$$

$$= a_k{}^{2-\epsilon} \int_{f(t_k)}^{f(t_k)+\delta} (y-f(t_k))^{1-\epsilon/2} dy,$$

$$= a_k{}^{2-\epsilon} \left. \frac{(y-f(t_k))^{\epsilon/2}}{\epsilon/2} \right|_{f(t_k)}^{f(t_k)+\delta},$$

$$= a_k{}^{2-\epsilon} \frac{(f(t_k)+\delta-f(t_k))^{\epsilon/2}}{\epsilon/2},$$

$$= \frac{2a_k^2\delta^{\epsilon/2}}{\epsilon}, \quad (17)$$

so that Eq. (14) becomes

$$\int_{f(t_k)}^{f(t_{k+1})-\delta} w_f(y)^{2-\epsilon}dy =$$

$$= \frac{2a_k^2\delta^{\epsilon/2}}{\epsilon} \pm \tilde{E}_k \frac{2a_k^2\delta^{\epsilon/2}}{\epsilon} + \tilde{\tilde{B}}_k,$$

$$= \frac{2a_k^2\delta^{\epsilon/2}}{\epsilon} \left[1 \pm \tilde{E}_k \right] + \tilde{\tilde{B}}_k, \quad (18)$$

which we sum over all minima to obtain

$$= \sum_{\substack{k \\ f''(t_k)>0}} \frac{2a_k^2\delta^{\epsilon/2}}{\epsilon} \left[1 \pm \tilde{E}_k \right] + \tilde{\tilde{B}}_k, \quad (19)$$

a sum of bounded and unbounded terms, whose unbounded term is computable directly from the experimentally accessible function $f(t)$ using $a_k = \sqrt{2/f''(t_k)} = \sqrt{2/|f''(t_k)|}$.

[Aside: for the maximum we have the asymptotic term

$$\int_{f(t_k)-\delta}^{f(t_k)} \left(\frac{a_k}{\sqrt{f(t_k)-y}} \right)^{2-\epsilon} dy. \quad (20)$$

So that the contribution to Eq. (6) from all of the maxima becomes

$$\int_{f(t_k)-\delta}^{f(t_k)} \left(\frac{a_k}{\sqrt{f(t_k)-y}} \right)^{2-\epsilon} dy =$$

$$= a_k{}^{2-\epsilon} \int_{f(t_k)-\delta}^{f(t_k)} (f(t_k)-y)^{1-\epsilon/2} dy,$$

$$= a_k{}^{2-\epsilon} \left. \frac{(f(t_k)-y)^{\epsilon/2}}{\epsilon/2} \right|_{f(t_k)-\delta}^{f(t_k)},$$

$$= a_k{}^{2-\epsilon} \frac{(f(t_k)-f(t_k)+\delta)^{\epsilon/2}}{\epsilon/2},$$

$$= \frac{2a_k^2\delta^{\epsilon/2}}{\epsilon}, \quad (21)$$

we now have a different expression for $a_k = \sqrt{-2/f''(t_k)} = \sqrt{2/|f''(t_k)|}$.]

Adding the contributions for the maxima and minima we obtain

$$\int_{f_{min}}^{f_{max}} w_f(y)^{2-\epsilon}dy =$$

$$= \sum_{\{t_k|f'(t_k)=0\}} \frac{2a_k^2\delta^{\epsilon/2}}{\epsilon} \left[1 \pm \tilde{E}_k \right] + \tilde{\tilde{B}}_k,$$

$$= \sum_{\{t_k|f'(t_k)=0\}} \frac{4\delta^{\epsilon/2}}{\epsilon|f''(t_k)|} \left[1 \pm \tilde{E}_k \right] + \tilde{\tilde{B}}_k. \quad (22)$$

Cross multiplying by ϵ

$$\epsilon \int_{f_{min}}^{f_{max}} w_f(y)^{2-\epsilon}dy =$$

$$= \sum_{\{t_k|f'(t_k)=0\}} \frac{4\delta^{\epsilon/2}}{|f''(t_k)|} \left[1 \pm \tilde{E}_k \right] + \epsilon\tilde{\tilde{B}}_k, \quad (23)$$

taking the logarithm of both sides and letting $\epsilon \to 0$ we have

$$\lim_{\epsilon \to 0}\left(\log \epsilon + \log\left[\int_{f_{min}}^{f_{max}} w_f(y)^{2-\epsilon} dy\right]\right) =$$

$$= \log\left[4 \sum_{\{t_k | f'(t_k)=0\}} \frac{1}{|f''(t_k)|}\left[1 \pm \tilde{E}_k\right]\right]. \qquad (24)$$

Now taking the limit $\delta \to 0$ so that the $\tilde{E}_k \to 0$ we obtain

$$\lim_{\epsilon \to 0}\left(\log \epsilon + \log\left[\int_{f_{min}}^{f_{max}} w_f(y)^{2-\epsilon} dy\right]\right) =$$

$$= \log\left[4 \sum_{\{t_k | f'(t_k)=0\}} \frac{1}{|f''(t_k)|}\right]. \qquad (25)$$

This shows that as $\epsilon \to 0$, the leading term in $\log \int w_f(y)^{2-\epsilon} dy$ always behaves like $\log 1/\epsilon$, regardless of $f(t)$; but the next term in the asymptotic expansion, the right-hand side of Eq. (25), does depend critically on $f(t)$, and is the quantity we seek.

Multiplying both sides by $1/(1-r) = 1/(1-2+\epsilon) \to -1$ and then cancelling minus signs on both sides of the equation, we obtain

$$\lim_{\epsilon \to 0}\left(-\log \epsilon - I_f(2-\epsilon)\right) =$$

$$= -\log\left[4 \sum_{\{t_k | f'(t_k)=0\}} \frac{1}{|f''(t_k)|}\right]. \qquad (26)$$

For imaging applications, where offset removal and rescaling are typically performed when pixel values are assigned, we define the new quantity

$$I_{f,\infty} \equiv -\lim_{\epsilon \to 0} I_f(2-\epsilon) - \log 4 + \log \epsilon$$

$$= \left[\sum_{\{t_k | f'(t_k)=0\}} \frac{1}{|f''(t_k)|}\right]. \qquad (27)$$

We will use this quantity to generate the images presented in the results section.

III. MATERIALS AND METHODS

A. Numerical Computation of $I_{f,\infty}$

Calculation of $I_{f,\infty}$ via Eq. (27) is accomplished by fitting a cubic spline to the experimentally acquired data array using a well-known algorithm, which returns the second derivative of the cubic spline (in an array having the same length as the experimental data) and initializes data structures suitable for rapid computation of its first derivative.[8] Subsequently, an array of corresponding first derivatives is computed and used to bracket the critical points of the spline (i.e., the zero crossings). Linear interpolation is then used to estimate the exact location of the bracketed zero crossings in order to obtain an algorithm suitable for real-time implementation in a medical
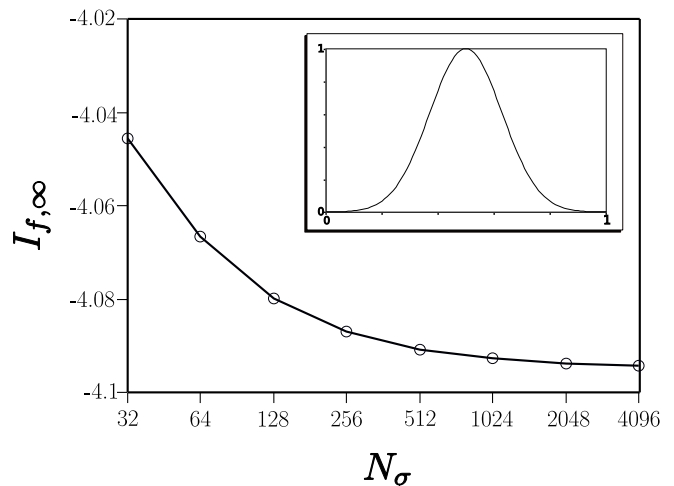

FIG. 4. Simulation for a noise free Gaussian pulse showing the dependence of $I_{f,\infty}$ on the number of sampled points N_σ.

imaging system. The total operation count is of order N_σ where N_σ is the number of points processed, is more than four orders of magnitude faster than the operation count $16384 N_\sigma$ required to compute $I_f(r)$ used in our previous study[1]. For comparison, we also note that the operation count required to produce the envelope of the same number of points (i.e., to produce a conventional B-Mode image) would be of order $N_\sigma \log(N_\sigma)$ since computation of the envelope requires use of the Fast Fourier Transform, for the value of $N_\sigma = 512$ used in our study below, this represents an increase in processing speed of roughly nine.

B. Simulations

The convergence properties, stability in the presence of noise, and effects of quantization error and sampling rate have been extensively evaluated using simulated data. Several types of waveforms have been investigated: Gaussian and parabolic waveforms, for which the exact value of $I_{f,\infty}$ may be computed and linear combinations of exponentially damped sine waves that qualitatively resemble backscattered ultrasonic waveforms. Several carefully chosen example simulations illustrate guidelines for application of our algorithm in order to avoid potential artifacts produced by experimental factors.

The first of these is Figure (4) which shows a plot of $I_{f,\infty}$ for a noise-free Gaussian pulse $f(t) = e^{-30(t-0.5)^2}$ for values of N_σ ranging from $32, 64, 128, ..., 8192$. Even at $N_\sigma = 32$ the estimated value of $I_{f,\infty}$ is within 1% of the exact value of $\log[1/60] = -4.094$. For moving window analysis of experimental data, N_σ is the length of the moving window. Choosing its length requires making trade-offs between sensitivity (smaller N_σ implying loss of sensitivity, but increased spatial resolution), noise level (smaller N_σ implying increased noise, but increased spatial resolution) and spatial resolution.
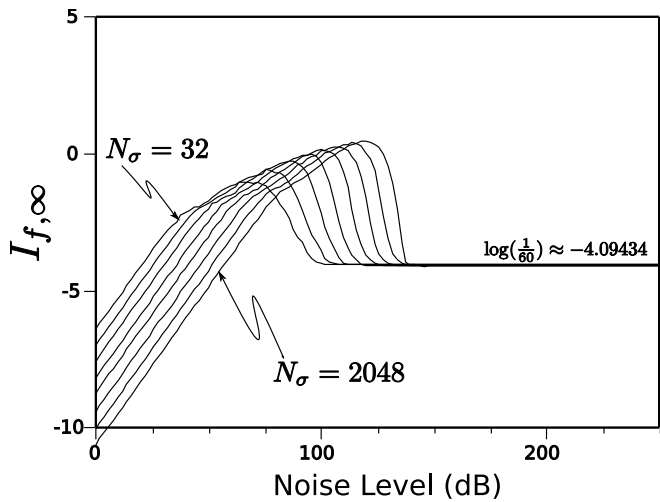
However, noise can have a significant effect on the cal-

FIG. 5. Simulation for a Gaussian pulse showing the dependence of $I_{f,\infty}$ on the number of sampled points N_σ and noise level.

FIG. 6. Simulation for an unquantized Gaussian modulated pulse showing the dependence on the number of sampled points N_σ and noise level.

culation of $I_{f,\infty}$. Figure (5) illustrates the impact of noise on the Gaussian pulse ($f(t) = e^{-30(t-0.5)^2}$) that was just discussed. As N_σ ranges from $32, 64, 128, ..., 8192$ and noise levels ranges from 0 to $150dB$, the calculated value of $I_{f,\infty}$ can vary by over 100% of its actual value. Eventually, as N_σ increases and the noise level drops, and our algorithm converges to a stable value. However, as the plots indicate, the noise requirements for a single peak function like the Gaussian peak are quite stringent, being greater than 100 dB to obtain 10% accuracy.

These requirements are less stringent if $f(t)$ has several critical points. An example is shown in Figure (6) which plots $I_{f,\infty}$ for values of N_σ ranging from $32, 64, 128, ..., 2048$, and for noise levels ranging from 0 to 150 dB for the Gaussian modulated pulse: $f(t) = e^{-10(t-0.5)^2} \sin(20\pi(t-0.5)) + 0.7\sin(20\pi(t-0.5)) + 0.7\sin(10\pi(t-0.5)))$. As the plots indicate the noise requirements for a multipeak peak waveform, $f(t)$, are far less stringent with 87% accuracy being obtained at about $20dB$ noise level for $N_\sigma = 512$ (plotted using a heavier line in the plot family since these parameters match values used in the experimental portion of our study).

Figure (7) shows a plot of $I_{f,\infty}$ for values of N_σ ranging from $32, 64, 128, ..., 8192$ for noise levels ranging from 0 to $150dB$ for the simulated pulse $f(t) = e^{-150(t-0.55)^2} \sin(40\pi(t-0.55)) + 0.7\sin(80\pi(t-0.55)) + 0.7\sin(20\pi(t-0.55)) + 0.03\sin(10\pi(t-0.55))$. The "exact" answer is -4.149073, found by running our algorithm with noise level set to zero, no quantization error, and $N_\sigma = 8192$, is also shown on the plot. The corresponding values of N_σ are indicated on the right side of the figure. For values of $N_\sigma \leq 512$ the error is less than 13%. We also note that for larger values of N_σ and lower levels of noise, our algorithm diverges with $I_{f,\infty}$ becoming large and positive. This occurs only in quantized simulations and is the result of the long perfectly flat segments in the quantized data. This is an easily detected fault and, since the $I_{f,\infty}$, images used in our experimental
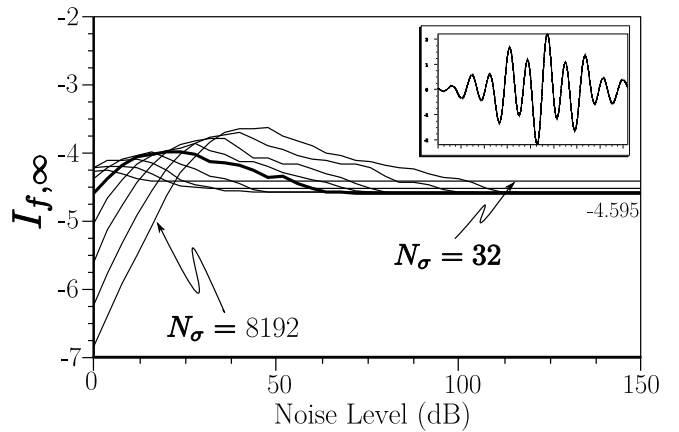
study had pixel values of approximately $7bits/symbol$ in magnitude on the regions used to estimate accumulation of targeted nanoparticles, can be ruled out as a possible artifact in our study.

C. Nanoparticles for molecular imaging

A cross-section of the spherical liquid nanoparticles used in our study is diagrammed in Figure (8). For *in vivo* imaging we formulated nanoparticles targeted to $\alpha_v\beta_3$-integrins of neovascularity in cancer by incorporating an "Arg-Gly-Asp" mimetic binding ligand into the lipid layer. Methods developed in our laboratories were used to prepare perfluorocarbon (perfluorooctylbromide, PFOB, which remains in a liquid state at body temperature and at the acoustic pressures used in this study[9]) emulsions encapsulated by a lipid-surfactant monolayer.[10,11] The nominal sizes for each formulation were measured with a submicron particle analyzer (Malvern Zetasizer, Malvern Instruments). Particle diameter was measured at $200\pm30nm$.

D. Animal model

The study was performed according to an approved animal protocol and in compliance with guidelines of the Washington University institutional animal care and use committee.

The model used is the transgenic K14-HPV16 mouse in which the ears typically exhibit squamous metaplasia, a pre-cancerous condition, associated with abundant neovasculature that expresses the $\alpha_v\beta_3$ integrin. Eight of these transgenic mice[12,13] were treated with 1.0 mg/kg i.v. of either $\alpha_v\beta_3$ -targeted nanoparticles (n=4) or untargeted nanoparticles (n=4) and imaged dynamically for one hour using a research ultrasound imager (Vevo 660 40MHz probe) modified to store digitized RF waveforms acquired at 0, 15, 30, and 60 minutes after injection of
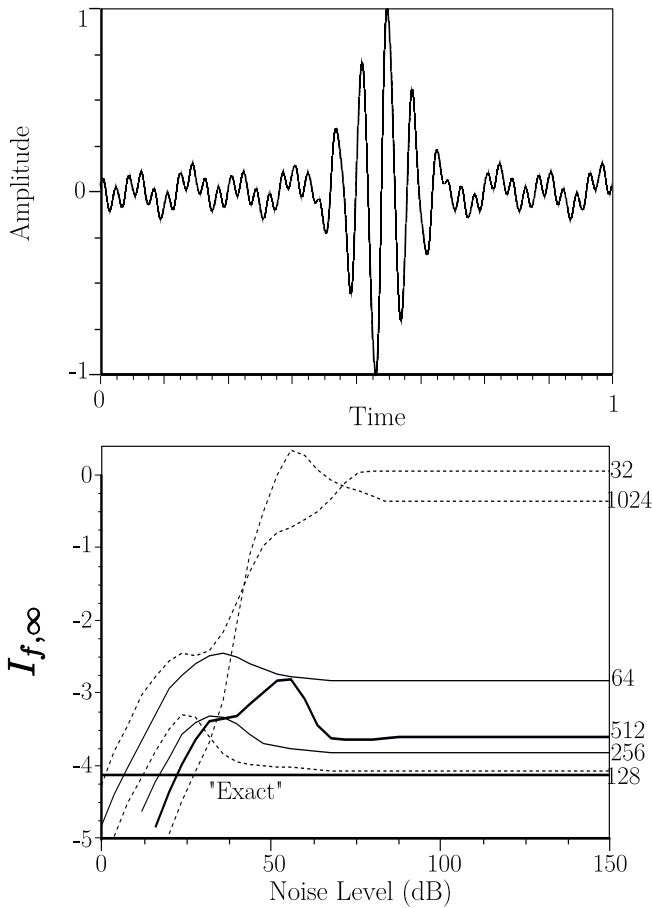
FIG. 7. Top panel: the simulated backscatter signal described in the text. Bottom panel: plot showing the dependence of $I_{f,\infty}$ on the number of sampled points N_σ and noise level at eight-bit quantization. The heavy black line labeled "Exact" is at 4.149, the limiting value of $I_{f,\infty}$ obtained from our algorithm in the unquantized, noise-free case with $N_\sigma = 8192$.

FIG. 8. A cross-sectional diagram of the nanoparticles used in our study.

nanoparticles. In both targeted and untargeted cases, the mouse was placed on a heated platform maintained at 37°C, and anesthesia was administered continuously with isoflurane gas (0.5%).

E. Ultrasonic Data Acquisition

A diagram of our apparatus is shown in Figure (9). Radio-frequency (RF) data were acquired with a research ultrasound system (Vevo 660, Visualsonics, Toronto, Canada), with an analog port and a sync port to permit digitization. The tumor was imaged with a 40 MHz single element "wobbler" probe and the RF data corresponding to single frames were stored on a hard disk for later off-line analysis. The frames (acquired at a rate of 40 Hz) consisted of 384 lines of 4096 eight-bit words acquired at a sampling rate of 500 MHz using a Gage CS82G digitizer card (connected to the analog-out and sync ports of the Vevo) in a controller PC. Each frame corresponds spatially to a region 0.8 cm wide and 0.3 cm deep.
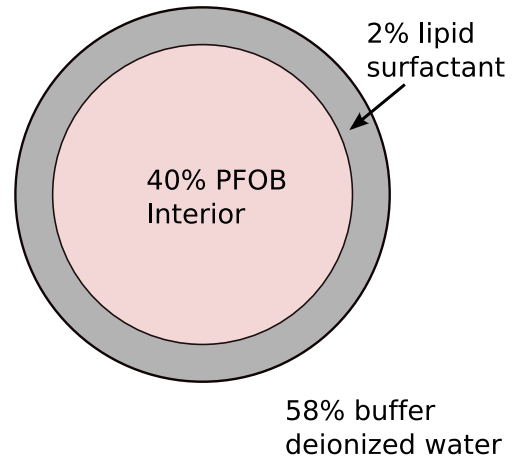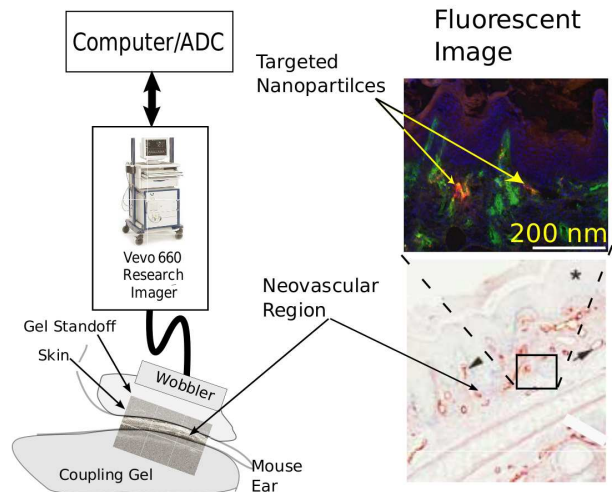
FIG. 9. A diagram of the apparatus used to acquire RF data backscattered from HPV mouse ears *in vivo* together with an histologically stained section of the ear indicating portions where $\alpha_v \beta_3$-targeted nanoparticles nanoparticles could adhere and a fluorescent image demonstrating presence of targeted nanoparticles.

The wobbler transducer used in this study is highly focused (3mm in diameter) with a focal length of 6 mm and a theoretical spot size of $80 \times 1100 \mu m$ (lateral beam width × depth of field at -6dB), so that the imager is most sensitive to changes occurring in the region swept out by the focal zone as the transducer is "wobbled". Accordingly, a gel standoff was used, as shown in Figure (9), so that this region would contain the mouse ear.

A close-up view showing the placement of transducer, gel standoff, and mouse ear is shown in the bottom of

the figure. Superposed on the diagram is a B-mode gray scale image (*i.e.*logarithm of the analytic signal magnitude). Labels indicate the location of skin (top of image insert), the structural cartilage in the middle of the ear, and a short distance below this, the echo from the skin at the bottom of the ear. Directly above this is an image of a histological specimen extracted from a HPV mouse model that has been magnified 20 times to permit better assessment of the thickness and architecture of the sites where $\alpha_v\beta_3$ targeted nanoparticle might attach (red by β_3 staining). Skin and tumor are both visible in the image. On either side of the cartilage (center band in image), extending to the dermal-epidermal junction, is the stroma. It is filled with neoangiogenic microvessels. These microvessels are also decorated with $\alpha_v\beta_3$ nanoparticles as indicated by the fluorescent image (labeled, in the upper right of the figure) of a bisected ear from an $\alpha_v\beta_3$-injected K14-HPV16 transgenic mouse. It is in this region that the $\alpha_v\beta_3$-targeted nanoparticles are expected to accumulate, as indicated by the presence of red β_3 stain in the magnified image of a histological specimen also shown in the image.
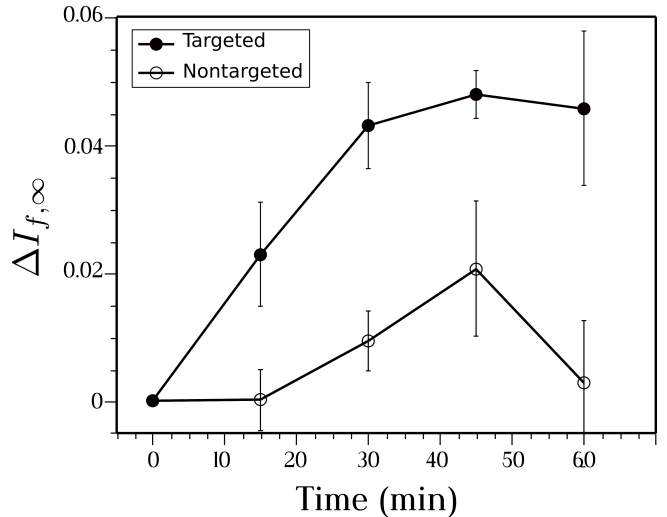

FIG. 10. $I_{f,\infty}$ image enhancement, *i.e.*, change relative to 0 minutes, obtained after injection of $\alpha_v\beta_3$ targeted nanoparticles(closed circles) and nontargeted nanoparticles (open circles) into from four HPV mice in each case.

F. Ultrasonic Data Processing

Each of the 384 RF lines in the data was first up-sampled from 4096 to 8192 points, using a cubic spline fit to the original data set in order to improve the stability of the thermodynamic receiver algorithms. As a by-product of this "order N_σ" algorithm is simultaneous output of a corresponding array of array second derivative values of the fit function[8]. Next, a moving window analysis was performed on the second derivative data set, using Eq. (27) to compute $I_{f,\infty}$, by moving a rectangular window (512 points long, 0.512 μs) in 0.064 μs steps (64 points), resulting in 121 window positions within the output data set. This produced an image for each time point in the experiment. The window length was chosen to match that used in previous studies[1,2], it corresponds to the heavy black curve shown in Figure (7). Analyses were also performed using window lengths of 256 (0.256 μs) and 128 points(0.256 μs). While they also produced statistically significant changes in $I_{f,\infty}$ versus time, post-injection, the resulting $I_{f,\infty}$ vs. time curves were noisier, and required one hour, post-injection, to exhibit statistically significant changes. As discussed previously, the optimum choice of window length requires trade-offs between sensitivity, noise level and spatial resolution. In the results section we discuss the 512 point moving window length results since they correspond most closely to previous results, which were supported by independent histological results[1,2], and produced images with sufficient spatial resolution to indentify relevant anatomical features in the mouse ear. Additionally, a major goal of this study was to assess the numerical stability of the algorithm, which is based on the second derivative of an experimentally measured data set, and thus contaminated by noise. Ordinarily, estimation of just the first derivative is difficult. However, in our application the effects of noise might be mitigated by two factors:

the second derivative is obtained from a global fit to the data, and the second derivative appears in the denominator of the expression for receiver output so that values of second derivative having large error are likely to make small contributions to the sum appearing in Eq. (27).

G. Image Processing

All RF data were processed off-line to reconstruct $I_{f,\infty}$ images. Subsequently, a histogram of pixel values for the composite of the 0, 15, 30, and 60 minute images was computed as described in previous papers[1,2]. Image segmentation of each type of image, at each time point in the experiment was then performed automatically using its corresponding histogram according to the following threshold criterion: the lowest 7 % of pixel values were classified as "targeted" tissue, while the remaining were classified as "untargeted" (histogram analysis was also performed using 90 and 87 percent thresholds, with 93 percent having the best statistical separation between time points). The mean value of pixels classified as "targeted" was computed at each time post-injection.

IV. RESULTS AND DISCUSSION

The results obtained after injection of targeted nanoparticles and nontargeted nanoparticles by $I_{f,\infty}$ receiver, are shown in Figure (10). Both curves show the time evolution of the change (relative to 0 minutes) in mean value of receiver output in the enhanced regions of images obtained from the four animals in the targeted and the four animals in the nontargeted groups. Standard error bars are shown with each point. At fifteen minutes the change in mean value if $I_{f,\infty}$ is more than two standard errors from zero, implying a statistical sig-

nificant at the 95% level. There is no statistically significant change in image brightness for the nontargeted nanoparticles group. As the results show, the algorithm for computation of $I_{f,\infty}$ is stable in the presence of experimental noise.

The results presented in this paper extend earlier studies where it was shown the an entropy based measure, H_f, was able to detect targeted nanoparticles in tumor neovasculature[2] after 30 minutes of accumulation time. Subsequently, the time required to detect targeted nanoparticles was reduced to 15 minutes using a generalization of entropy, $I_f(r)$, with $r = 1.99$, although the time required for signal analysis was greatly increased[1]. In the current study based on $I_{f,\infty}$, the analysis time has been reduced from days to minutes using an algorithm suitable for real-time implementation, while maintaining sensitivity that permits detection of nanoparticle accumulation at 15 minutes.

Real-time performance appears to have been purchased at the price of reduced statistical sensitivity, in view of prior observation that $I_f(1.99)$ separated by over five standard errors from 0 at 15 minutes[1] as compared to the 2 standard error separation obtained with the real-time receiver (see Figure (10)). It is possible that preprocessing of the data by bandpass filtering might improve the statistical performance of the algorithm without significant increase in computational overhead. This will be studied in a future report.

Acknowledgments

[1] M. S. Hughes, J. E. McCarthy, J. N. Marsh, J. M. Arbeit, R. G. Neumann, R. W. Fuhrhop, K. D. Wallace, T. Thomas, J. Smith, K. Agyem, D. R. Znidersic, B. N. Maurizi, S. L. Baldwin, G. M. Lanza, and S. A. Wickline, "Application of Renyi entropy to detect subtle changes in scattering architecture", Journal of the Acoustical Society of America **In press** (2009).

[2] M. S. Hughes, J. E. McCarthy, J. N. Marsh, J. M. Arbeit, R. G. Neumann, R. W. Fuhrhop, K. D. Wallace, D. R. Znidersic, B. N. Maurizi, S. L. Baldwin, G. M. Lanza, and S. A. Wickline, "Properties of an entropy-based signal receiver with an application to ultrasonic molecular imaging", Journal of the Acoustical Society of America **121**, 3542–3557 (2007).

[3] R. S. Bucy and P. D. Joseph, *Filtering for Stochastic Processes with Applications to Guidance* (Chelsea Publishing Company, New York, NY) (1987).

[4] N. Wiener, *Extrapolation, interpolation, and smoothing of stationary time series : with engineering applications* (M.I.T. Press, Cambridge, MA) (1949).

[5] U. Grenander and M. Rosenblatt, *Stastical Analysis of Stationary Time Series* (Chelsea Publishing Company, New York, NY) (1984).

[6] T. M. Cover and J. A. Thomas, *Elements of Information Theory* (wiley-Interscience, New York) (1991).

[7] R. Tolman, *The Principles of Stastical Mechanics* (Dover Press, New York, NY) (1979).

[8] W. H. Press, S. A. Teukolsky, W. T. Vetterling, and B. P. Flannery, *Numerical recipes in C*, 2nd edition (Cambridge University press, Cambridge) (1992).

[9] M. S. Hughes, J. N. Marsh, J. Arbeit, R. Neumann, R. W. Fuhrhop, G. M. Lanza, and S. A. Wickline, "Ultrasonic molecular imaging of primordial angiogenic vessels in rabbit and mouse models with $\alpha_v\beta_3$-integrin targeted nanoparticles using information-theoretic signal detection: Results at high frequency and in the clinical diagnostic frequency range", Proceedings of the 2005 I.E.E.E. Ultrasonics Symposium (2005).

[10] S. Flacke, S. Fischer, M. J. Scott, R. J. Fuhrhop, J. S. Allen, M. McLean, P. Winter, G. A. Sicard, P. J. Gaffney, S. A. Wickline, and G. M. Lanza, "Novel MRI contrast agent for molecular imaging of fibrin implications for detecting vulnerable plaques", Circulation **104**, 1280–1285 (2001).

[11] G. M. Lanza, K. D. Wallace, M. J. Scott, W. P. Cacheris, D. R. Abendschein, D. H. Christy, A. M. Sharkey, J. G. Miller, P. J. Gaffney, and S. A. Wickline, "A novel site-targeted ultrasonic contrast agent with broad biomedical application", Circulation **94**, 3334–3340 (1996).

[12] J. M. Arbeit, R. R. Riley, B. Huey, C. Porter, G. Kelloff, R. Lubet, J. M. Ward, and D. Pinkel, " chemoprevention of epidermal carcinogenesis in k14-hpv16 transgenic mice", Cancer Research **59**, 3610–3620 (1999).

[13] J. M. Arbeit, K. Mnger, P. M. Howley, and D. Hanahan, "Progressive squamous epithelial neoplasia in k14-human papillomavirus type 16 transgenic mice", Journal of Virology **68**, 4358–4368 (1994).